



Cite this: *RSC Adv.*, 2023, 13, 5173

Waste sawdust-based composite as an interfacial evaporator for efficient solar steam generation

Marimuthu Rengasamy and Kamatchi Rajaram *

Interfacial evaporation is the technology of localizing heat energy at the air–water interface and is used for getting potable water from salty or seawater effectively. In this work, we introduce a novel interfacial evaporator by blending different weight ratios of waste sawdust (1 g, 2 g, 3 g and 4 g) with bisphenol-A epoxy resin (LY556) and triethyltetramine hardener (HY951). The fabricated epoxy hardener sawdust (EHS) composite material was subjected to various characterizations for the possibility of using it in solar steam generation. Consequently, EHS displayed high light absorption, amorphous structure, functional groups, and large number of pores. The main objective of the study was to investigate interfacial solar steam generation with and without interfacial evaporators (EHS-1g, EHS-2g, EHS-3g, and EHS-4g) under indoor conditions. The maximum mass loss of water, evaporation rate and evaporation efficiency were found to be 4.5 g, 1.398 kg m^{−2} h^{−1}, and 92.99%, respectively, for the EHS-4g evaporator. The salinity of the distilled condensed water was measured and was below the WHO standards. The results are due to (i) the large number of cross-linked porous structures used to permeate water at the evaporative surface by capillary action, (ii) low thermal conductivity of the composite that offers an efficient broad and strong light absorption, and (iii) existence of a larger hydraulic diameter and small tortuosity of pores, which reduces the salt ion penetration distance and dispatch back to bulk water.

Received 1st December 2022
Accepted 17th January 2023

DOI: 10.1039/d2ra07654c

rsc.li/rsc-advances

Introduction

Potable water is essential for all people to live on Earth. It is unfortunate that the amount of fresh water for every individual keeps decreasing due to the fast growth of industrialisation, population, modern society and natural droughts. It has been reported that almost 29% people are unable to obtain pure water and 6% deaths occur in developing countries from drinking impure water. Although many natural water resources are available globally, they are not directly utilized for drinking due to the presence of pesticides, suspended particles, anionic pollutants, colloidal materials, heavy metals, non-metallic substances, microorganisms, and various dissolved metallic substances. Furthermore, the natural water resources may be polluted and everyone will necessitate a substitute source to acquire water and fulfill their basic requirements by 2050.^{1–5}

To rectify this omnipresent issue, many new technologies such as multi-effect distillation technology, flash distillation, and reverse osmosis have been developed to obtain pure drinking water. However, salt mitigation of seawater affects the efficiency and life of the equipment. In addition, membrane fouling and high energy demand are long-term problems in the reverse osmosis system. Reverse osmosis and multi-effect distillation also consume significant power input of about 5

and 8 kW h m^{−2}, respectively. Therefore, they are unsuitable for offshore regions, villages, and remote off-grid areas. Thus, it is time to seek a sustainable desalination technology that is low cost, scalable, portable and achieves peak output with low energy input.^{6–9} Solar energy is one of the indispensable, sustainable and renewable energy technologies. Currently, solar energy is employed in the photochemical, photovoltaic and photothermal fields. Photothermal processes convert light to heat through reflection, absorption and high temperature. Solar thermal distillation is one of the best conventional methods for steam generation. Here, solar light is directly used to heat water, which gets evaporated and is collected by the condensation process.^{10–12}

In recent years, interfacial solar steam generation (ISSG) has emerged as a potential and environmentally friendly solution to the problem of a lack of water among a variety of constantly developing technologies. It is the process of absorbing a large amount of solar energy using carbon-based materials, porous polymers, metal nanoparticles, black semiconductors and other absorber materials.^{13,14} The vapour is formed on the interface surface by highly localising the solar energy where bulk water heating is hindered. The total amount of incident light is utilized to heat the top surface of the substrate. So, the unwanted heat loss is minimized. At the beginning of World War II, U.S. military pilots and sailors used this technology to produce drinking water in ocean areas. Here, the first aid kit was fabricated using a black wet cotton towel and plastic bag.

School of Mechanical Engineering, Vellore Institute of Technology, Vellore – 632014, Tamil Nadu, India. E-mail: rkkamatchi@gmail.com



Later, the process was categorized as interfacial solar steam generation.^{15,16} The first interfacial solar evaporator was made of a hydrophilic porous structure substrate that assisted in transporting water, while it floated on the water surface.¹⁷ Li *et al.*¹⁸ used rice straw-based membranes to investigate the performance, and found a maximum of 75.8% evaporation efficiency. Liu *et al.*¹⁹ experimented with a carbonised sawdust-based evaporator in ISSG, and obtained an efficiency of about 77.64%. Xue *et al.*²⁰ conducted ISSG using treated wood with fire. They reported an evaporation efficiency of 72% at 1 kW m⁻². On the other hand, Dandan *et al.*²¹ investigated Ni-NiO_x/Ni foam in ISSG and attained 1.41 kg m⁻² h⁻¹ in evaporation rate. Wei H. *et al.*²² showed an evaporation rate of 1.73 kg m⁻² h⁻¹ with Cu_xS/Cu foam. Over the last decade, different substrates like aerogels, paper, gauze, wood, and sawdust have been introduced in ISSG due to their good insulating property, biodegradability and low cost.²³ Among all, wood has better properties like low thermal conductivity, accessibility and high water transfer. The structure of the interfacial evaporator also plays a vital role in evaporation efficiency. This method can be applied in various applications, such as sewage disposal, oil-water separation, electricity generation, and waste sterilisation.²⁰

Currently, blending natural fibres into polymers is widely used for various applications like building, shipping, and packing industries. Due to their unique properties such as being lightweight, contributing less pollution and having a higher fibre content, natural fibres are chosen rather than synthetic fibres. In the past few years, natural fibres like sawdust, teak, hemp, jute, cotton, sisal, pine, flax and broom have been incorporated with polyolefins, polystyrene and epoxy resins to fabricate thermoset and thermoplastic matrices.²⁴ Natural biopolymers like polydopamine and melanin-based bio polymers have also been used in ISSG due to their effective hydrophilicity, non-toxic, biodegradability and noble photo-thermal conversion efficiency.²⁵ Open-celled microcellular polymer materials have a large number of similar-sized microporous structures that allow for particles, fluids, gas and sound to pass through them, and are further used in many applications.²⁶ Huang *et al.*²⁷ fabricated polystyrene/lignocelluloses skeleton-based membranes and found an evaporation efficiency of 85.5% under 1.5 sun illuminations. Li *et al.*²⁸ obtained an evaporation efficiency of 77% under 1 sun irradiation when PDA-coated raw wood was used as an evaporator. Juan *et al.*²⁹ experimentally investigated the ISSG process using an attapulgite/poly acrylamide composite. They found an evaporation efficiency of 85%. Lifang *et al.*³⁰ fabricated a 2D electrospun nanofibrous membrane by blending polyacrylonitrile and bisphenol epoxy resin. They showed that the fabricated membrane has high porosity and can be used in ISSG, resulting in an evaporation rate of 2.70 kg m⁻² h⁻¹. Liu *et al.*³¹ experimented with the ISSG process using a membrane (poly(3,4-ethylenedioxythiophene) and polyetheramide-modified cation exchange resin) and a maximum evaporation rate of 1.42 kg m⁻² per hour was achieved.

It was found from the literature that a limited number of research works on polymer-based composite have experimented

with solar steam generation. Most of the research works followed the chemical blowing method for the preparation of polymer composites. It is also a time-consuming and costly process. The novelty of the present work is to prepare a low-cost, facile and self-floating salt rejection epoxy/hardener/sawdust polymer composite as an interfacial evaporator for enhancing the performance of solar steam generation. The fabricated composite has a hierarchically cross-linked porous structure and more active sites that facilitate fast water permeation.

The present investigation aimed to fabricate interfacial evaporators with different weight ratios of sawdust and epoxy resin. These interfacial evaporators were then used in the interfacial steam generation process at indoor conditions. The champion device resulted in a maximum mass loss of 4.5 g, evaporation rate of 1.39 kg m⁻² h⁻¹ and solar thermal efficiency of 92.99% under 1 sun illumination. Furthermore, the concentration of heavy metal ions was reduced considerably below WHO standards. As a result, it has been demonstrated that the interfacial evaporators show significant promise for producing solar vapour and may be useful for various sun-heating applications, including solar distillation, power generation and sterilisation.

Experimental section

Materials

Coconut tree sawdust was collected from the local woodcutter shop and dried in sunlight to remove the moisture content. Epoxy resin (bisphenol-A) – LY 556 and Aradur Hardener curing agent (triethyltetramine) HY - 951 were purchased from the market. Seawater was collected from Marina Beach, Chennai, India (latitude-130 03' 15.05" N, and longitude-800 17' 1.25" E). Stereolithography (SLA) of 3D printing filament with 1.75 mm in diameter was purchased from Sigma-Aldrich. Sawdust was chosen as the filler material because of its low thermal conductivity nature, non-toxicity, low cost and waste product.

Fabrication of circular-type epoxy/hardener/sawdust composite

In this study, a 2 : 1 ratio of epoxy resin and hardener was taken to fabricate the polymer-based interfacial evaporator. First, a polyethylene cup was taken and cleaned with distilled water to remove impurities and dust. With the help of disuse paper, the moisture content was removed from the cup. Next, epoxy resin was poured into the cup and added with 1 g of sawdust. The hardener was added and stirred for about 2 min using a glass stirring rod. Then, the mixture was kept in an ideal place for 10 min. The thickness and size of the composites were swelled due to exothermic reactions. The mechanism of curing was mainly due to the substitution reaction of the hardener-HY 951. The presence of nucleophilic NH₂ in the hardener attacked the electrophilic carbon of the C–O bond of the epoxide ring of bisphenol A-LY 556, which led to breaking the chain and resulted in ring opening. This process continued until the hierarchically cross-linked structure formation occurred. The chemical and cross-linked structure of the composite is



illustrated in Fig. 1. Here, the molecules of the compositions react and a slight increase in temperature was observed. During this process, the air was mechanically whipped or beaten into the epoxy/hardener/sawdust mixture and formed micro and macro froths. The polymerization of the resin mixture resulted in irregular pores, like elliptical and spherical pores, which were connected by pore throats. After reducing the temperature of the composite, it was taken out from the polyethylene cup. Then, the required size of the composite (Dia: 65 mm and thickness: 10 mm) was cut and used for the interfacial solar steam generation process. It was named as epoxy/hardener/sawdust-1 g composite (EHS-1g). In order to hold the developed composite material, a 3D-printed ring was fabricated using SLA material. The diameter and thickness of the 3D-printed ring were 65 mm and 7.5 mm, respectively.

Similarly, the same quantity of epoxy/hardener was combined with sawdust at various weight ratios (2 g, 3 g, and 4 g) to develop the different composites, which were named as EHS-2g, EHS-3g and EHS-4g, respectively. The fabrication process of the epoxy/hardener/sawdust composites is shown in Fig. 2. During the above processes, we identified that the increase in the amount of sawdust reduced the formation of froths and the size of pores.

Steam generation experimental setup

The solar simulator-based steam generation process is shown in Fig. 3. Here, the solar simulator was placed on top of the bulk seawater surface. The incident light intensity was measured by a pyranometer and maintained at 1 sun illumination. The steam generation process was conducted without and with

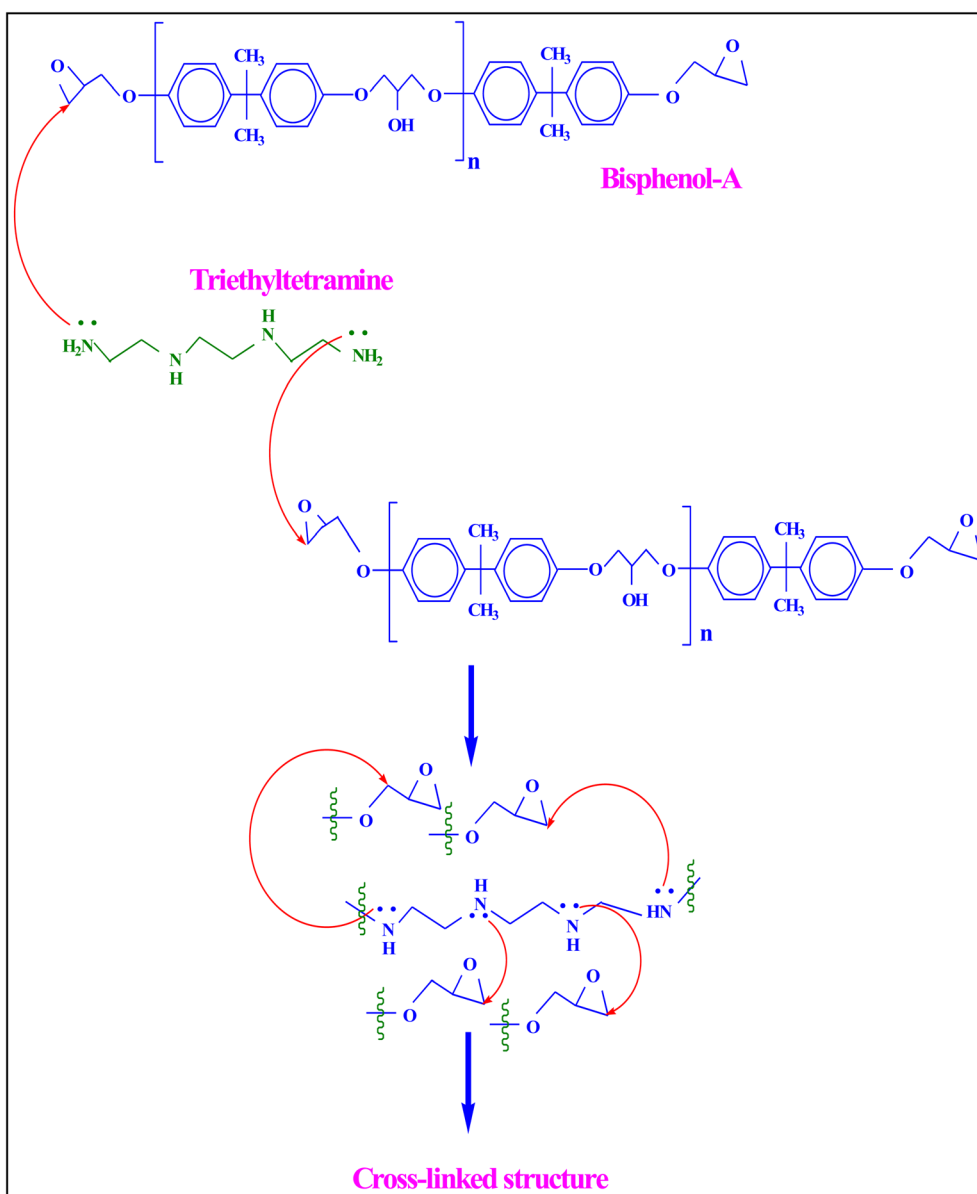


Fig. 1 Chemical structure and cross-linked structure of the epoxy/hardener/sawdust composite.



Fig. 2 Fabrication of the circular type epoxy/hardener/sawdust composite.

(EHS-1g, EHS-2g, EHS-3g, and EHS-4g) evaporated medium. When the EHS (epoxy/hardener/sawdust) evaporator was floated on the water surface, it acted as a water transporting medium for steam generation. Temperature distribution from the evaporator surface to water was recorded using a thermal image camera. The steam generation process was executed for 60 min, and the mass loss of water was noted every 5 min using a weighing machine.

Characterization

The 3D printing material was developed using a WANHAO Duplicator 4S instrument. A UV-Vis-NIR spectrometer (Jasco V-670) was used to evaluate the light absorption capacity of the prepared materials over the range of 250 to 400 nm. Phase analysis of the EHS evaporator was analysed by X-ray diffraction (XRD) D8 advanced instrument (Make: Bruker-Germany). Functional groups were determined by an attenuated total reflection Fourier transform infrared (ATR-FTIR) spectroscopy instrument (Make: Thermo Fisher Sci., US) in the infrared wavelength region. Field emission scanning electron microscopy (FE-SEM) was used to study the surface morphology of the composite. The thermal conductivity of the sample was estimated using a KD2 Pro instrument (Make: Decagon Device, INC, US). The surface temperature of the evaporator during steam generation was recorded using a thermal image FLIR camera (Model: T1020-12-NIST, India). A Citizen CY 204 (Make: kalpanaTechnolab, India) instrument was used to measure the mass loss of water. The ion concentrations of the impure and collected water were measured by atomic absorption spectroscopy (Model: Varian AA 240, make: SpectraLab scientific Inc,

Canada) and flame photometer instruments (Make: Systronics, Model: 128).

Results and discussion

Characterizations of the EHS composite

UV-vis absorbance studies. Optical absorbance spectra of the prepared composites were measured using UV-vis spectrometer at room temperature. The UV-vis absorbance spectra of EHS-1g, EHS-2g, EHS-3g and EHS-4g are shown in Fig. 4. The absorbance of each composite gradually increased in the ultraviolet region (200–290 nm), and then decreased gradually up to 400 nm. From the observations, the EHS-4g composite showed better results in the spectral range of 200–400 nm. In the EHS-4g composite evaporator, the amount of sawdust was higher than other composite evaporators. So, the sawdust was distributed evenly in the composite evaporator. This may be the reason for the better absorbance in EHS-4g compared to the other evaporators. It was also noticed that adding sawdust content into the epoxy resin enhanced the light absorption behaviour in the UV region.

XRD analysis. The crystalline phases of the composite materials were derived using XRD analysis. Fig. 5 depicts the XRD analysis of the EHS-1g, EHS-2g, EHS-3g and EHS-4g composites, showing the 2θ peak value in the range of 10–30°. The obtained results are well matched with the existing literature, showing that the amorphous structure of epoxy forms a peak value (2θ) between 10 and 30°. As observed from Fig. 5, no new peaks are formed by varying sawdust ratios in the epoxy. It also shows that no distinct physical structure is found in place during the formation of the composite material.





Fig. 3 Solar steam generation experimental setup.

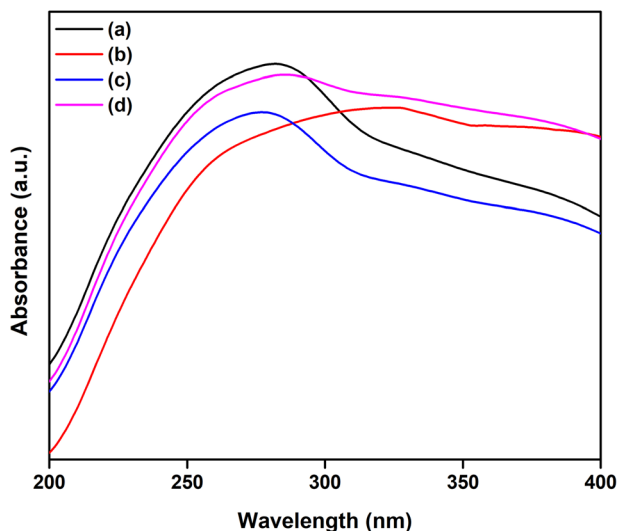


Fig. 4 UV-vis analysis of (a) EHS-1g, (b) EHS-2g, (c) EHS-3g and (d) EHS-4g.

FT-IR analysis. The surface functional groups and bonding characteristics of sawdust, EHS-1g, EHS-2g, EHS-3g and EHS-4g interfacial evaporators are assessed using FT-IR spectroscopy,

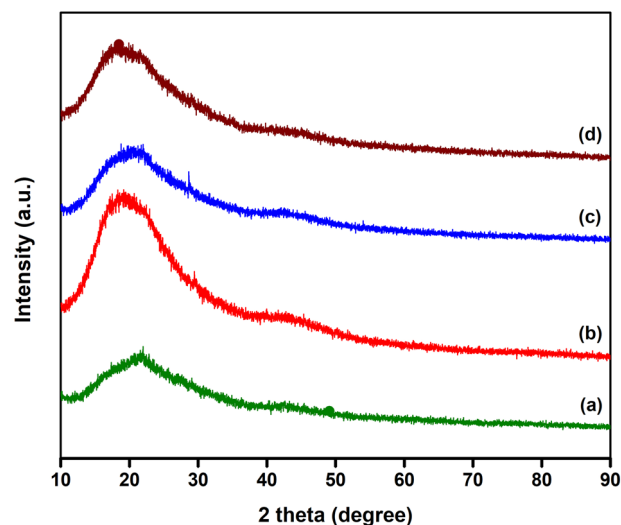


Fig. 5 XRD analysis of (a) EHS-1g, (b) EHS-2g, (c) EHS-3g and (d) EHS-4g.

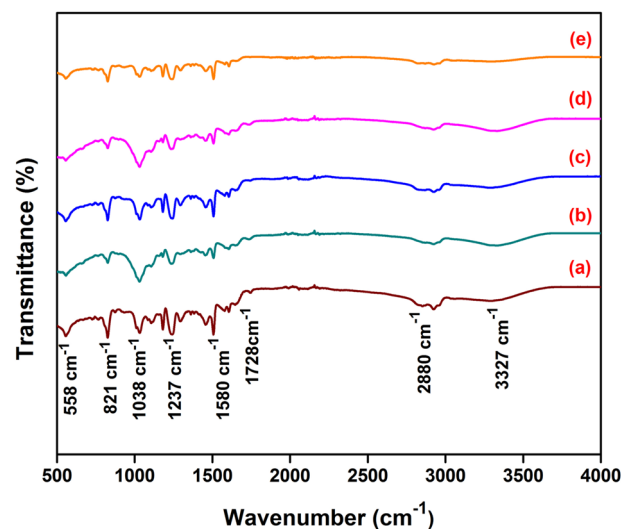


Fig. 6 FT-IR analysis of (a) sawdust, (b) EHS-1g, (c) EHS-2g, (d) EHS-3g and (e) EHS-4g.

and illustrated in Fig. 6. The halogen groups C-X are detected at the peaks of 558 and 1038 cm^{-1} . The hemicellulose C-O stretching vibration is observed at 1237 cm^{-1} . The COO-deprotonated carboxylate groups correspond to the peak at 1580 cm^{-1} . The stretching vibrations of carboxylic acid and ester C-O are found at 1728 cm^{-1} . The peaks at 2880 cm^{-1} correspond to the CH_3 stretching. In addition, cellulose, hemicelluloses and lignin components are found in the samples. At 3327 cm^{-1} , the hydroxyl group (O-H) is observed. These findings show that no additional peaks have been found, indicating no chemical interactions between epoxy and sawdust.^{34,35}

Morphology analysis. The surface morphology of the EHS composite-based materials was studied using FE-SEM, and is shown in Fig. 7. Different magnification levels have been used



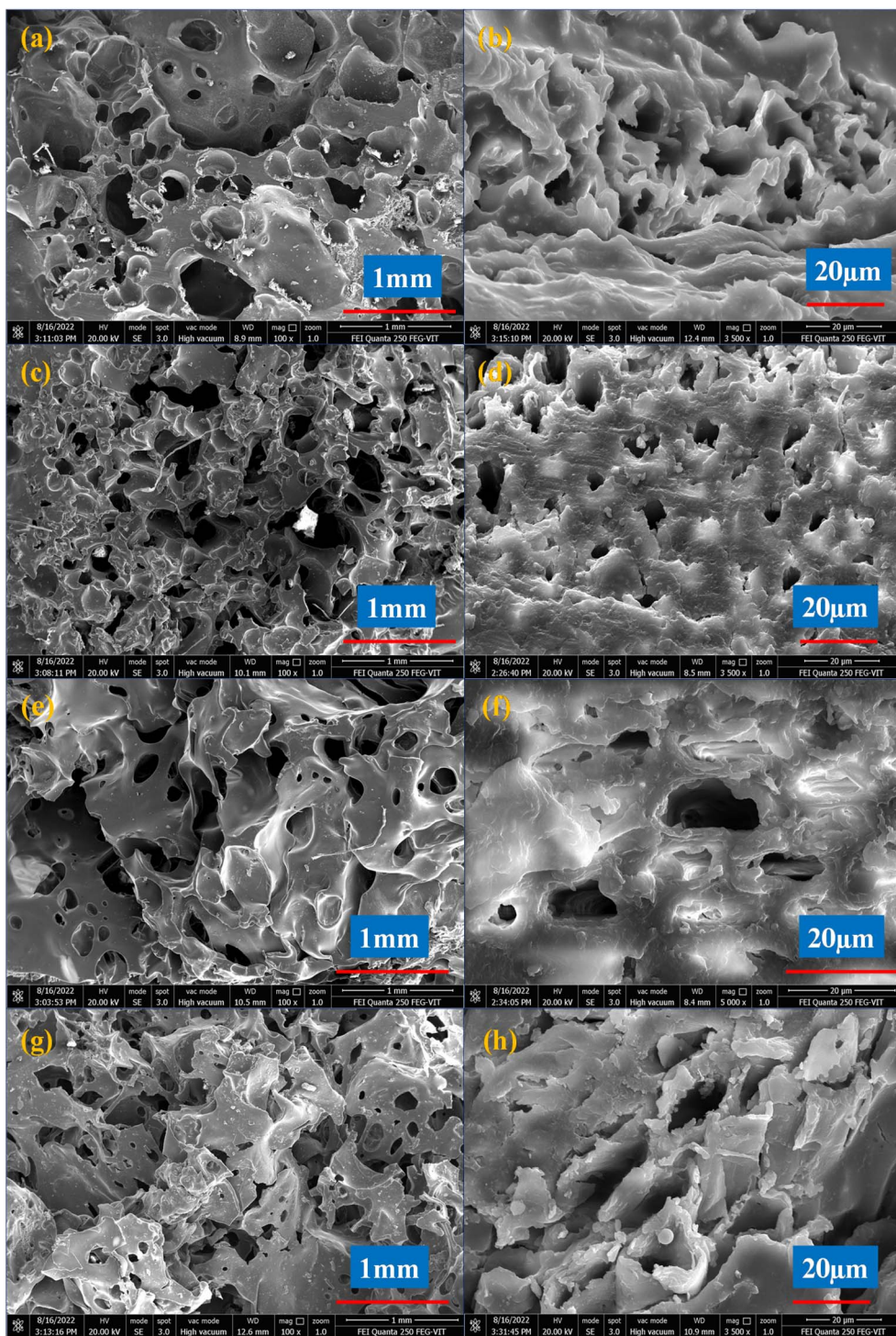


Fig. 7 FE-SEM images of the (a and b) EHS-1g, (c and d) EHS-2g, (e and f) EHS-3g, and (g and h) EHS-4g composites for the magnification ranges of 1 mm and 20 μm .

to study the morphological behaviour of EHS-1g (a, b), EHS-2g (c, d), EHS-3g (e, f) and EHS-4g (g, h), respectively. At 1 mm magnification, numerous micro- and macro-sized porous are observed. At 20 μm , the composite materials have spherical and elliptical structures connected through water channels, and promote water transportation continuously from bulk water to

the water-air interface. The diameter of the pores of the composite is also measured, and varied from 19 to 200 μm (Fig. 13c). The addition of sawdust into the epoxy resin affects the blowing process of the composite. It reduces the formation of froths and diameter of pores. Hence, small cavities and tortuosity is produced in the fabricated composites.



Thermal conductivity analysis. The thermal conductivity of the composite materials was measured at room temperature using a KD2 Pro analyzer. The thermal conductivity values of EHS-1g, EHS-2g, EHS-3g and EHS-4g are 0.277, 0.216, 0.148 and 0.095 W mK⁻¹, respectively. These results showed that the thermal conductivity of the epoxy/hardener/sawdust composite materials was decreased. The epoxy resin had a low thermal conductivity of 0.10 W mK⁻¹.³⁶ The addition of sawdust into the epoxy was found to reduce the thermal conductivity of the composite material. The reduction in the thermal conductivity may be due to the existence of air voids on the evaporators that occurred during the curing process.²⁵ Among these results, the EHS-4g composite has lower thermal conductivity than the others, as it has a higher weight ratio of sawdust added with epoxy.

Thermal image camera analysis. The surface temperatures of bulk water and interfacial evaporators (EHS-1g, EHS-2g, EHS-3g

and EHS-4g) were measured using an infrared (IR) camera. The images were captured during the steam generation process at 0, 15, 30, 45 and 60 min under 1 sun irradiation, shown in Fig. 8. Initially, the experiment was carried out without an interfacial evaporator under indoor conditions. The variations in temperatures were captured at every 15 min intervals, as depicted in Fig. 8a. The surface temperature increased linearly with time, and was measured as 54.80, 67.10, 68.80, 69.10 and 70.00 °C, respectively. The temperature distribution of the bulk water gradually increased from top surface to bottom surface with very little variation. Due to heat losses brought on by bulk heating, the water did not readily evaporate. Fig. 8b–e illustrates the surface temperature of EHS-1g, EHS-2g, EHS-3g and EHS-4g, respectively. Over a period of time, there was not much change in temperature at the top surface of the interfacial evaporators. The temperature distribution from the top evaporated surface to water with and without an interfacial evaporator floating on

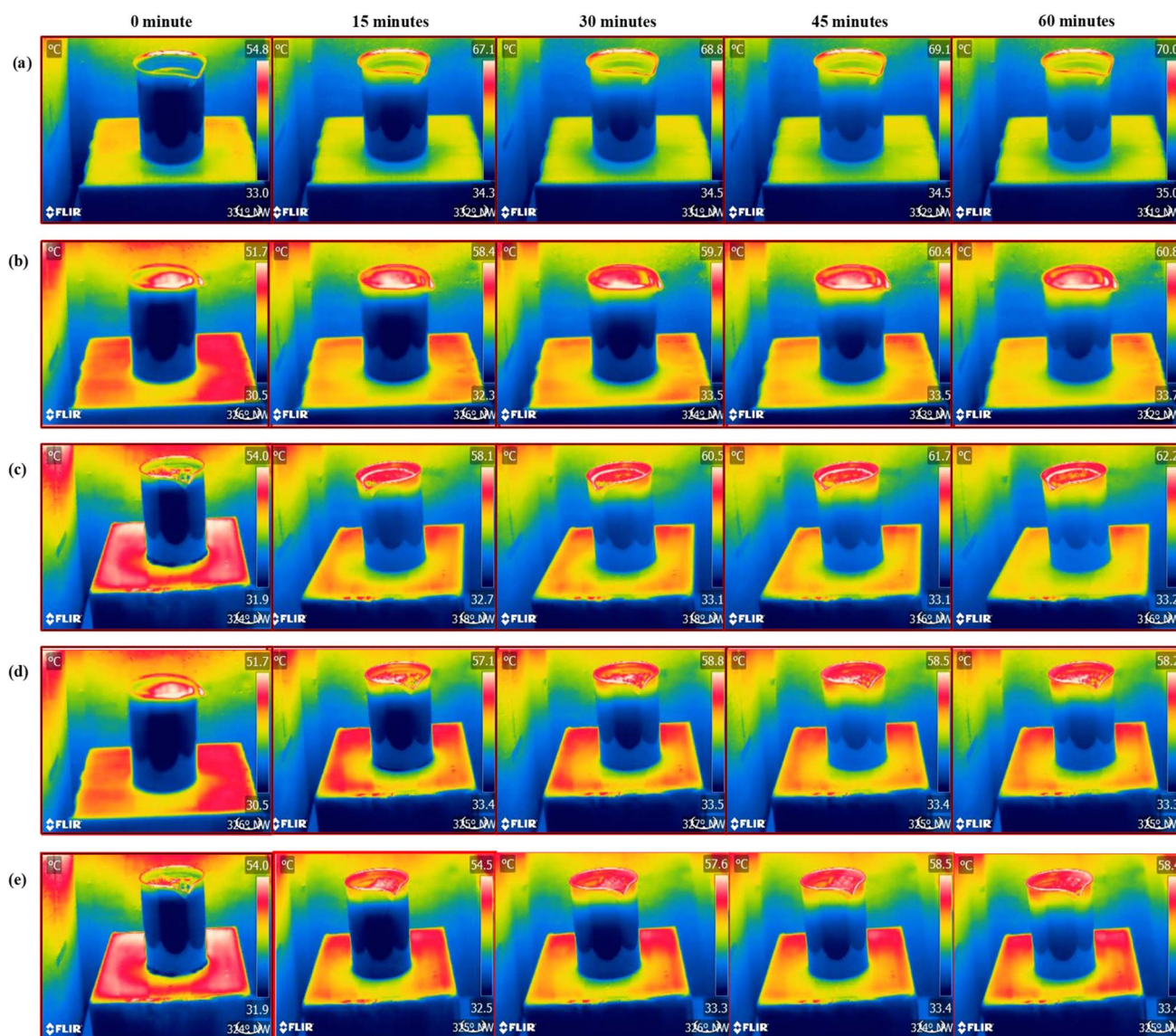


Fig. 8 Thermal image analysis: (a) without evaporator, (b) EHS-1g, (c) EHS-2g, (d) EHS-3g and (e) EHS-4g at 0, 15, 30, 45 and 60 min.

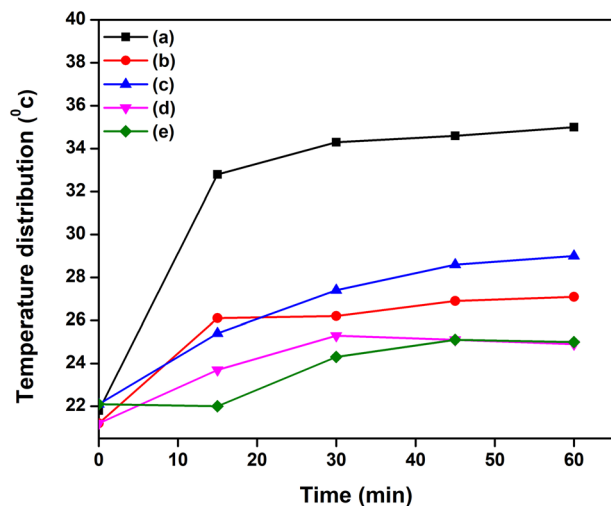


Fig. 9 Temperature distribution analysis: (a) without evaporator, (b) EHS-1g, (c) EHS-2g, (d) EHS-3g, and (e) EHS-4g at 0, 15, 30, 45 and 60 min.

the seawater is also represented in Fig. 9. It shows that the EHS-4g evaporator gives a low-temperature distribution compared to others. This is because the increased amount of sawdust leads to an enhanced water absorption rate.³⁷ So, the large amount of water transportation is effectively achieved by capillary action, and moves to the evaporation surface. As the thermal conductivity of the EHS-4g evaporator is low, the temperature and heat available at the top surface are almost utilized to evaporate the water. It is because of this that the temperature distribution of the EHS-4g evaporator is low, leading to a higher evaporation rate.

Solar steam generation performance analysis. Steam generation is the process of converting incident light to heat energy. The molecular force of attraction at the bottom of the bulk water is higher than the top surface of the water. The kinetic energy of the surface molecules increases with the absorption of heat energy, and finally escapes as vapour. During steam generation, water gets evaporated below its boiling point. The solar steam generation efficiency (η) is calculated using eqn (1):³⁸

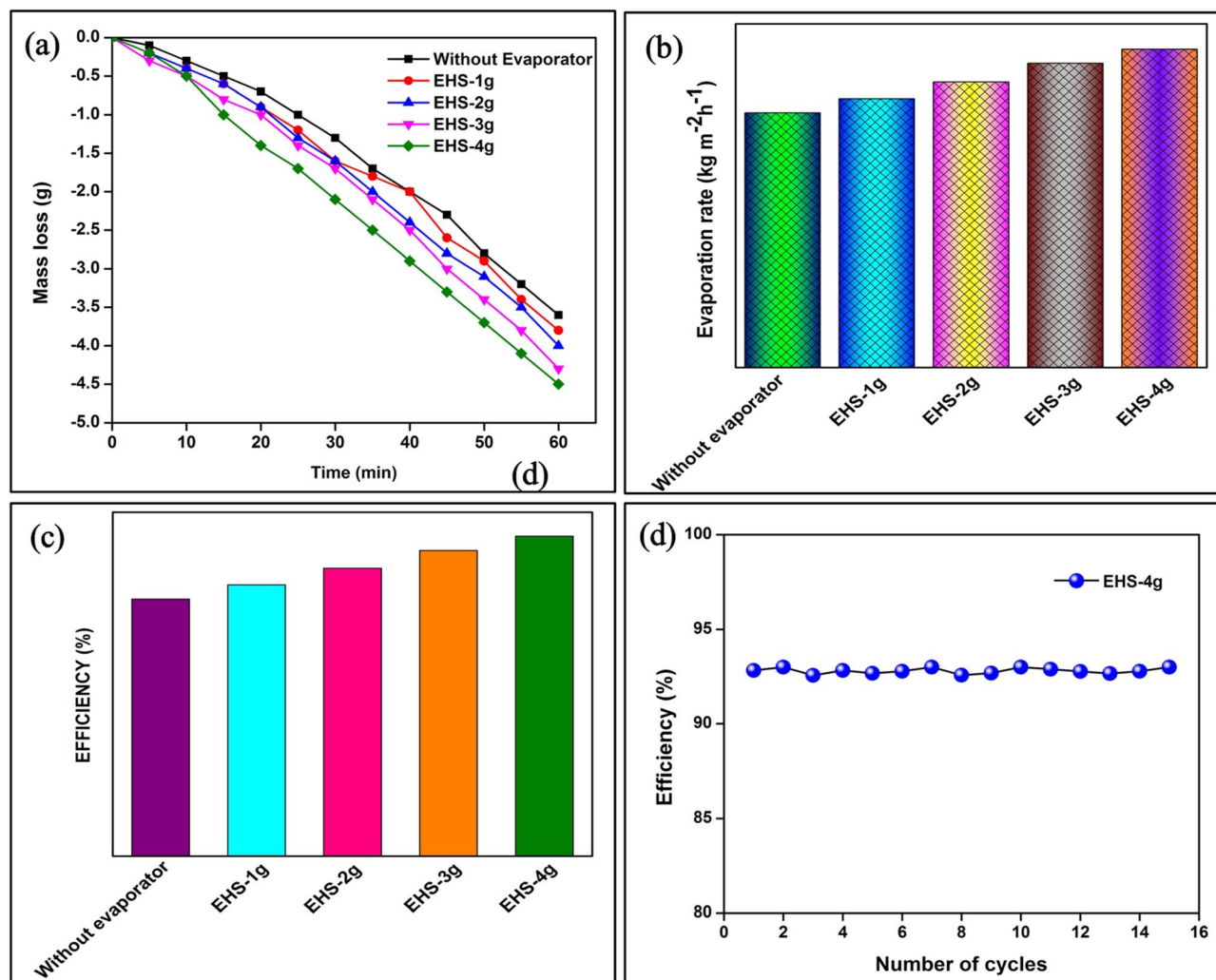


Fig. 10 Steam generation analysis of (a) mass loss, (b) evaporation rate, (c) efficiency and (d) solar steam generation efficiency of the EHS-4g for 15 cycles.



$$\eta = \frac{\dot{m}h_v}{q} \quad (1)$$

where h_v – enthalpy of water (J kg^{-1}); q – intensity of solar light (W m^{-2}); and \dot{m} – evaporation rate of water ($\text{kg m}^{-2} \text{h}^{-1}$).

The mass loss, evaporation rate and evaporation efficiency of water without and with interfacial evaporators are shown in Fig. 10a–c. Without an interfacial evaporator, the obtained mass loss, evaporation rate and efficiency of water are 3.6 g, $1.119 \text{ kg m}^{-2} \text{h}^{-1}$ and 74.76%, respectively. In general, the supply of heat input to water is lost by conduction, convection and radiation.³⁹ So, the bulk water heating gives insufficient output. In contrast, the interfacial evaporators (such as EHS-1g, EHS-2g, EHS-3g and EHS-4g) have evaporation rates of 1.181, 1.253, 1.336, and $1.398 \text{ kg m}^{-2} \text{h}^{-1}$, and the corresponding efficiencies are 78.93%, 83.65%, 88.85% and 92.99%, respectively. The obtained results are much higher than that without an interfacial evaporator case. In order to evaluate the repeatability and durability of the EHS-4g evaporator, the experiments were conducted with the existing setup for 15 repetitive cycles. Fig. 10d depicts the evaporation efficiency of the repetitive cycles. It can be seen that the efficiency did not change much in all the cycles, which confirms that the EHS-4g evaporator is highly stable. The mass loss of water of EHS-1g, EHS-2g, EHS-3g and EHS-4g is 3.8, 4.0, 4.3 and 4.5 g, respectively. The mass loss of water increases with the addition of sawdust into the epoxy resin. Here, EHS has numerous pores and each pore is interconnected with the water channel. With the presence of small cavities in this channel, water refilling at the evaporation surface is achieved quickly. The low thermal conductivity of the interfacial evaporator suppresses the heat losses and avoids heat distribution to the

bulk fluid. It promotes decreasing losses *via* conduction, convection and radiation. So, the total amount of heat is utilized for heating the top surface of the water.

Salt accumulation in the evaporation process is the major concern for the ISSG process, as it blocks the water transport channel. This further reduces the mass loss, evaporation rate and efficiency. Fig. 11 illustrates the prevention of salt accumulation at the evaporative surface of EHS-4g composite before (dry) and after (wet) steam generation process. It can be seen that there is no salt accumulated on the evaporative surface for after steam generation process.

Here, the high porosity and small tortuosity effect of the evaporator help to increase the salt interchange of bulk water and supply water continuously to the evaporation surface through plentiful water channels. Due to the larger size of the pores, the hydraulic diameter is increased, which aids in supplying more amounts of water flows in a single channel. Hence, salt growth is restricted and the salt emigrate rate at the evaporative surface is reduced.

We suggest that the following may be the reasons for obtaining the enhanced steam generation: (i) the EHS-4g composite material absorbs a greater amount of solar irradiation and converts heat energy effectively; (ii) as the composite material has a good number of pores, it aids in achieving good capillary action and water refilling at the evaporative surface productively; (iii) the fabricated composite material develops an indirect water path, which gives effective heat treatment at the air–water interface and encouraging interfacial solar steam generation; (iv) As the EHS evaporator has low thermal conductivity (0.095 W mK^{-1}), it restricts the heating of the bulk fluid.

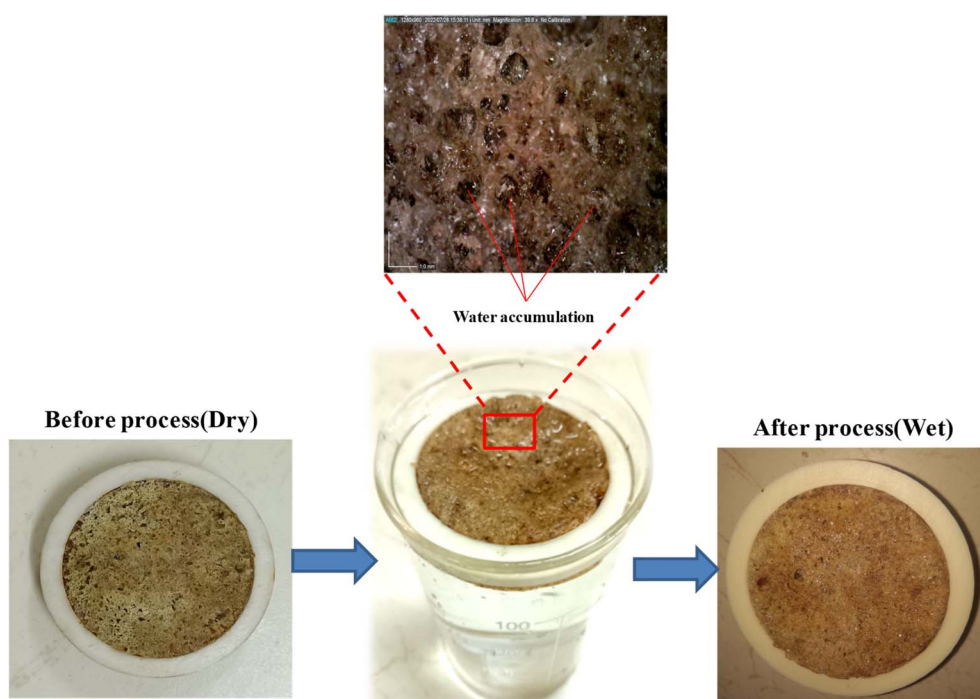


Fig. 11 Prevention of salt accumulation at the evaporative surface of the EHS-4g composite – before and after the steam generation process.



Water quality testing

UV analysis of water. UV absorption analysis was carried out for seawater and condensed water, and is represented in Fig. 11a. Due to the presence of heavy metals and impurities in seawater, absorption peaks are seen in the UV region. As seen from Fig. 12a, the highest absorption peak is obtained at ~ 211 nm for seawater and ~ 204 nm for condensed water. The absorption peak of condensed water is lower than that for seawater. This shows that the presence of ions/element concentration is decreased in the condensed water.

Analysis of heavy metals ions. The presence of heavy metals (magnesium (Mg), chromium (Cr), manganese (Mn), nickel (Ni), lead (Pb), cadmium (Cd), cobalt (Co), iron (Fe), zinc (Zn), copper (Cu) and sodium (Na)) at high concentrations affects the liver, kidney, brain, placenta, bones, peripheral nervous system, bloody urine, skin ulcer, and can cause breathing problems.^{40–42} Hence, the World Health Organization (WHO) recommends a standard level of heavy metals in drinking water.

The ISSG has the ability to produce clean and potable water, leaving behind inorganic heavy metals like Mg, Cr, Mn, Ni, Pb, Cd, Co, Fe, Zn, Cu, and Na. The presence of heavy metals in the water sample was examined using an atomic absorption

spectroscopy instrument (Make: Varian Inc, India; Model: AA 240). The sodium ion was measured using a flame photometer (Make: Systronics, Model: 128) instrument. Fig. 12b–d depicts the sample of seawater and condensed water. As observed from Fig. 12b–d, the sample of seawater has a higher heavy metal concentration above the drinking water standard, as suggested by WHO. As a result, Cd, Co, Cr, Mn, Ni, Pb, Fe, Zn, Cu, Mg and Na ions concentrations are reduced by orders of magnitude to 16.3, 3.8, 12.5, 3.9, 6.85, 10, 8.67, 80.48, 88.1, 745 and 433 mg L⁻¹, respectively, in the condensed water. It was observed that the amount of ion concentration in the evaporated water has reduced considerably, and meets the safe-drinking water levels provided by the WHO standard.^{31,42} We suggest the reason for the decreasing ion concentrations as follows: The fabricated composite material has twists, bends and a crooked porous structure. When the water passes through these structures, the tortuosity effect arises. Therefore, the movement of heavy metal ions is hindered during evaporation by a microporous interfacial evaporating medium. Because the size of the salt ions is larger than that of water molecules, the penetration of salt ions is trapped on the evaporative medium. Numerous pores on the interfacial medium generated a larger

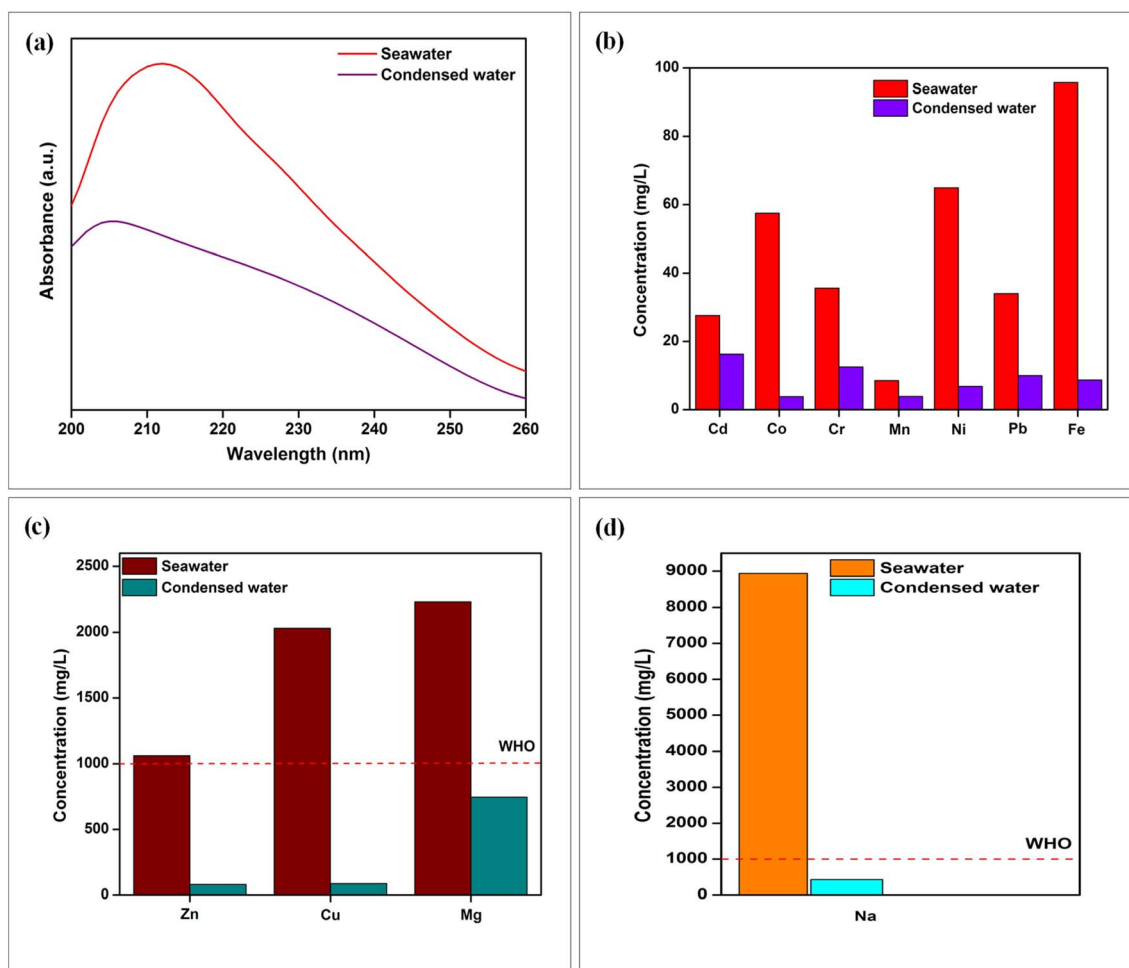


Fig. 12 (a) UV analysis, and (b)–(d) atomic absorption spectroscopy and flame photometer analysis: seawater and condensed water.



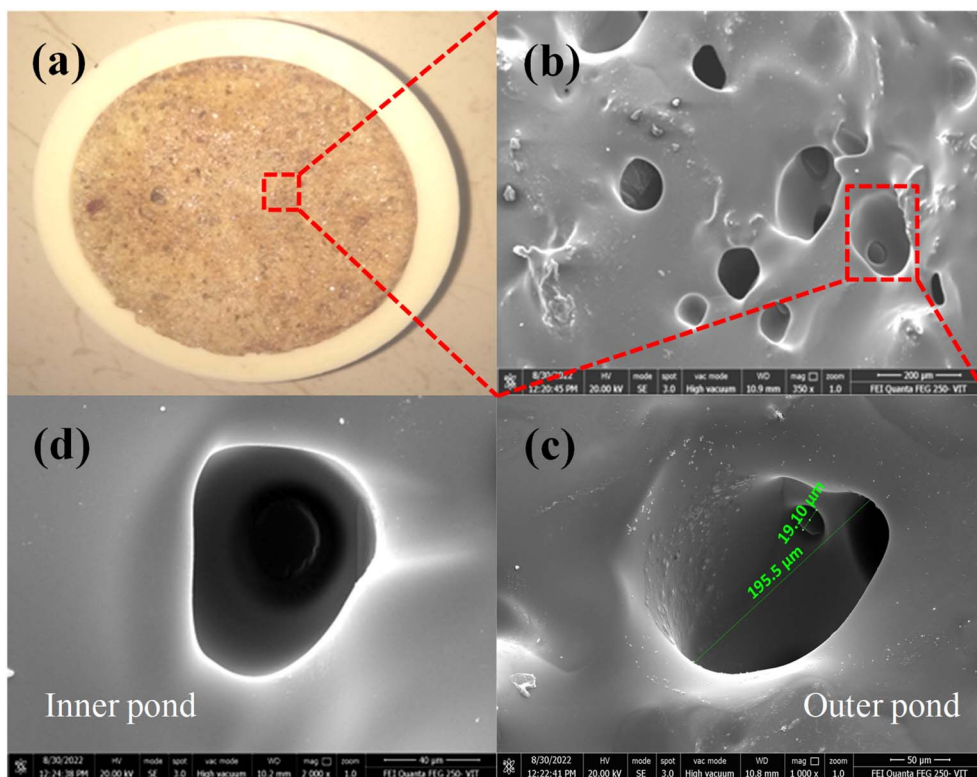


Fig. 13 Possible water transportation and steam generation mechanism (a) EHS-4g evaporator (b) FESEM image for 200 μm (c) outer pond (d) inner pond.

hydraulic diameter, which increases the amount of water permeation from the bottom to the evaporative surface. So, the salt ions emigration distance is reduced and goes back to the bottom water. This prevents salt accumulation at the evaporative surface, while using high-salinity of water. For those above reasons, the EHS-4g evaporator offers efficient antifouling capability for long term.

Possible water transportation and steam generation mechanism. In this work, the interfacial evaporator floats on the top surface of the bulk water. As the thermal conductivity of the interfacial evaporator is low, the heat loss due to conduction, convection and radiation can be minimized. It was observed that the water absorption rate of the composite depends on the amount of sawdust present in the composite. This is mainly due to the existence of hydroxyl groups on the sawdust. Fig. 13 depicts the fabricated EHS-4g and its FE-SEM images. As observed from the FE-SEM images, a pond-like cross-linked porous structure is seen on the top surface of the composite. A single pond consists of interconnected inner and outer ponds. When the EHS composite floats on the water, the water first fills the inner pond due to capillary action, and the spill out water reaches the outer pond for evaporation. Therefore, this inner pond continuously supplies water and acts as a reservoir for evaporation. This kind of structure reduces the time taken for the emigration of water from the bottom to reach the top surface for evaporation. When the temperature of water at the top surface of the interfacial evaporator is increased by 1 sun irradiation, a significant rise in saturation pressure will occur.

In particular, more water needs to enter the ambient space to achieve this balance, leading to a higher evaporation rate. This is the reason why the maximum mass loss of 4.5 g, evaporation rate of $1.398 \text{ kg m}^{-2} \text{ h}^{-1}$ and evaporation efficiency of 92.99% was observed for the EHS-4g sample.

Conclusion

In summary, the fabricated brand-new epoxy/hardener/sawdust (EHS-1g, EHS-2g, EHS-3g and EHS-4g) composite-based interfacial evaporators have been tested for the efficient and stable solar-driven interfacial steam generation process. This study experimentally proved that the EHS-4g composite evaporator has small cavities in the water transporting channels, which aids the replacement of water at the evaporation surface effectively. Large hydraulic diameters and small tortuosity of pores hinder salt accumulation at the top surface and balance the water transportation. The low thermal conductivity of the interfacial evaporators also prohibits the heat distribution from the radiated surface to bulk water. The EHS-4g composite evaporators have the antifouling capability, and provide quick, affordable manufacturing and scalability that offer promising strategies for sustainable freshwater production from seawater, especially water with high salinity. The EHS-4g composite evaporator showed excellent solar vapour generation potential, and is probably suitable for other applications, such as sterilizing, desalination and distillation. In the future, we have a plan to coat eco-friendly nanomaterials over the evaporative surface

of the EHS-4g composite evaporator for highly efficient solar steam generation.

Conflicts of interest

There are no conflicts to declare.

References

- 1 J. O. Duruibe, M. O. C. Ogwuegbu and J. N. Egwurugwu, *Int. J. Phys. Sci.*, 2007, **2**(5), 112–118.
- 2 B. C. Kross, *J. Prev. Med.*, 2002, **10**(1), 3–10.
- 3 A. K. Kaviti, A. S. Ram, A. Aruna Kumari and S. Hussain, *Mater. Today: Proc.*, 2021, **44**, 282–288.
- 4 S. P. Suriyaraj and R. Selvakumar, *RSC Adv.*, 2016, **6**(13), 10565–10583.
- 5 P. K. Singh, P. K. S. Rathore and S. K. Shukla, *Int. J. Energy Res.*, 2022, **46**(2), 937–951.
- 6 C. Zhang, H. Q. Liang, Z. K. Xu and Z. Wang, *Adv. Sci.*, 2019, **6**(18), 1970111.
- 7 L. Li, T. Hu, A. Li and J. Zhang, *Chem. Eng. J.*, 2021, **422**, 129998.
- 8 S. Tiwari and P. K. S. Rathore, *Mater. Today: Proc.*, 2022, DOI: [10.1016/j.matpr.2022.08.048](https://doi.org/10.1016/j.matpr.2022.08.048).
- 9 V. K. Chauhan, S. K. Shukla, J. V. Tirkey and P. K. S. Rathore, *J. Cleaner Prod.*, 2021, **284**, 124719.
- 10 H. M. Qiblawey and F. Banat, *J. Environ. Prot.*, 2008, **220**(1–3), 633–644.
- 11 Z. Li, C. Wang, T. Lei, H. Ma, J. Su, S. Ling and W. Wang, *Adv. Sustainable Syst.*, 2019, **3**(4), 1800144.
- 12 V. K. Chauhan, S. K. Shukla and P. K. S. Rathore, *J. Energy Storage*, 2021, **47**, 103578.
- 13 K. Xu, C. Wang, Z. Li, S. Wu and J. Wang, *Adv. Funct. Mater.*, 2021, **31**(8), 1–26.
- 14 Z. Wang, M. Han, F. He, S. Peng, S. B. Darling and Y. Li, *Nano Energy*, 2020, **74**, 104886.
- 15 F. Tao, Y. Zhang, K. Yin, S. Cao, X. Chang, Y. Lei, D. Wang, R. Fan, L. Dong, Y. Yin and X. Chen, *Sustainable Energy Fuels*, 2018, **2**(12), 2762–2769.
- 16 X. Luo, J. Shi, C. Zhao, Z. Luo, X. Gu and H. Bao, *Appl. Energy*, 2021, **302**, 117581.
- 17 H. Ghasemi, N. George, A. M. Marconnet, J. Loomis, S. Yerci, N. Miljkovic and G. Chen, *Nat. Commun.*, 2014, **5**, 1–7.
- 18 Q. Fang, T. Li, Z. Chen, H. Lin, P. Wang and F. Liu, *ACS Appl. Mater. Interfaces*, 2019, **11**(11), 10672–10679.
- 19 S. Liu, C. Huang, X. Luo and C. Guo, *Appl. Energy*, 2019, **239**, 504–513.
- 20 G. Xue, *ACS Appl. Mater. Interfaces*, 2017, **9**(17), 15052–15057.
- 21 D. Wu, D. Qu, W. Jiang, G. Chen, L. An, C. Zhuang and Z. Sun, *J. Mater. Chem. A*, 2019, **7**(14), 8485–8490.
- 22 W. Huang, P. Su, Y. Cao, C. Li, D. Chen, X. Tian, Y. Su, B. Qiao, J. Tu and X. Wang, *Nano Energy*, 2020, **69**, 104465.
- 23 M. M. Ghafurian, M. R. Malmir, Z. Akbari, M. Vafaei, H. Niazmand, E. K. Goharshadi, A. Ebrahimi and O. Mahian, *Energy*, 2022, **244**, 123146.
- 24 R. Chandra Mohapatra, A. Mishra and B. Bhushan Choudhury, *Am. J. Mech. Eng.*, 2014, **2**(4), 114–119.
- 25 X. Xu, S. Ozden, N. Bizmark, C. B. Arnold, S. S. Datta and R. D. Priestley, *Adv. Mater.*, 2021, **33**(18), 1–9.
- 26 D. Doermann and J. F. Sacadura, *J. Heat Transfer*, 1996, **118**(1), 88–93.
- 27 Q. Huang, C. Du, C. Guo, C. Huang and X. Wang, *Appl. Therm. Eng.*, 2021, **187**, 116515.
- 28 Y. Zou, P. Yang, L. Yang, N. Li, G. Duan, X. Liu and Y. Li, *Polymers*, 2021, **217**, 123464.
- 29 J. Jia, W. Liang, H. Sun, Z. Zhu, C. Wang and A. Li, *Chem. Eng. J.*, 2019, **361**, 999–1006.
- 30 L. Qiao, N. Li, L. Luo, J. He, Y. Lin, J. Li, L. Yu, C. Guo, P. Murto and X. Xu, *J. Mater. Chem. A*, 2021, **9**(15), 9692–9705.
- 31 C. Liu, Y. Peng, C. Cai, J. Zhang and X. Zhao, *J. Environ. Chem. Eng.*, 2021, **9**(4), 105272.
- 32 S. M. Moosavi Nejad, M. Madhoushi, D. Rasouli and M. Vakili, *J. Wood For. Sci. Technol.*, 2017, **23**, 313–328.
- 33 H. Alhumade, H. Rezk, A. M. Nassef and M. Al-Dhaifallah, *IEEE Access*, 2019, **7**, 100899–100909.
- 34 (a) N. U. Rahman, I. Ullah, S. Alam, M. S. Khan, L. A. Shah, I. Zekker, J. Burlakovs, A. Kallistova, N. Pimenov, Z. Vincevica-Gaile and Y. Jani, *Water*, 2021, **13**(15), 2136; (b) H. Yang, Y. Wang, Z. Liu, D. Liang, F. Liu, W. Zhang, X. Di, C. Wang, S. H. Ho and W. H. Chen, *J. Bioresour. Bioprod.*, 2017, **4**, 1–2.
- 35 S. Yu, J. W. Lee, T. H. Han, C. Park, Y. Kwon, S. M. Hong and C. M. Koo, *ACS Appl. Mater. Interfaces*, 2013, **5**(22), 11618–11622.
- 36 N. Kumari, M. Paswan and K. Prasad, *Mater. Today: Proc.*, 2021, **49**, 1719–1722.
- 37 Y. Xu, J. Yin, J. Wang and X. Wang, *Rev. Adv. Mater. Sci.*, 2019, **58**(1), 226–247.
- 38 S. L. Wu, H. Chen, H. L. Wang, X. Chen, H. C. Yang and S. B. Darling, *Environ. Sci.: Water Res. Technol.*, 2021, **7**(1), 24–39.
- 39 W. G. S. Martin, *Environ. Sci. Technol.*, 2001, **15**, 1–6.
- 40 J. Hussain, I. Husain, M. Arif and N. Gupta, *Appl. Water Sci.*, 2017, **7**(8), 4539–4548.
- 41 M. Kumar, S. Singh and R. K. Mahajan, *Environ. Monit. Assess.*, 2006, **112**(1–3), 283–292.
- 42 H. Li, D. Jia, M. Ding, L. Zhou, K. Wang, J. Liu, C. Y. Liu and C. Li, *Sol. RRL*, 2021, **5**(8), 1–11.

